

Published in final edited form as:

Microvasc Res. 2014 July ; 94: 17–27. doi:10.1016/j.mvr.2014.04.008.

Characterization of nanoparticle delivery in microcirculation using a microfluidic device

Antony Thomas¹, Jifu Tan², and Yaling Liu^{1,2,*}

¹Bioengineering program Lehigh University, Bethlehem, PA 18015, USA

²Department of Mechanical Engineering and Mechanics Lehigh University, Bethlehem, PA 18015, USA

Abstract

This work focuses on the characterization of particle delivery in microcirculation through a microfluidic device. In microvasculature the vessel size is comparable to that of red blood cells (RBCs) and the existence of blood cells largely influences the dispersion and binding distribution of drug loaded particles. The geometry of the microvasculature leads to non-uniform particle distribution and affects the particle binding characteristics. We perform an *in vitro* study in a microfluidic chip with micro vessel mimicking channels having a rectangular cross section. Various factors that influence particle distribution and delivery such as the vessel geometry, shear rate, blood cells, particle size, particle antibody density are considered in this study. Around 10% higher particle binding density is observed at bifurcation regions of the mimetic microvasculature geometry compared to straight regions. Particle binding density is found to decrease with increased shear rates. RBCs enhance particle binding for both 210 nm and 2 μ m particles for shear rates between 200-1600 s^{-1} studied. The particle binding density increases about 2-3 times and 6-10 times when flowing in whole blood at 25% RBC concentration compared to the pure particle case, for 210 nm and 2 μ m particles respectively. With RBCs, the binding enhancement is more significant for 2 μ m particles than that for 210 nm particles, which indicates an enhanced size dependent exclusion of 2 μ m particles from the channel centre to the cell free layer (CFL). Increased particle antibody coating density leads to higher particle binding density for both 210 nm and 2 μ m particles.

Keywords

Microcirculation; Microvasculature; Microfluidic chip; Particle distribution; Red blood cells; Shear rate; Bifurcation region

© 2014 Elsevier Inc. All rights reserved.

*Corresponding author. Tel.: +1-610-758-5839; fax: +1-610-758-6224. Postal address: 19 Memorial Dr W, Packard Lab, Lehigh University, Bethlehem, PA 18015 yal310@lehigh.edu. ant210@lehigh.edu (A. Thomas), jit310@lehigh.edu (J. Tan).

Publisher's Disclaimer: This is a PDF file of an unedited manuscript that has been accepted for publication. As a service to our customers we are providing this early version of the manuscript. The manuscript will undergo copyediting, typesetting, and review of the resulting proof before it is published in its final citable form. Please note that during the production process errors may be discovered which could affect the content, and all legal disclaimers that apply to the journal pertain.

Introduction

Various techniques in targeted drug delivery have been developed in recent years to reduce side effects, toxicity, and drug dosage [1]. The use of particles as drug carrier helps in targeted delivery and release of drugs at disease region, serving the dual role of diagnosis and therapy [2-3]. Nanoparticles (NPs) in the form of liposomes, dendrimers, micelles and polymers, as well as the more conventional and inorganic carbon, silica, iron and gold NPs are being widely used as drug carriers [4]. The uptake efficacy of NP based drug carriers is higher compared to their larger micron scale counterparts, which are easily cleared off by the human mononuclear phagocyte system. NPs also have larger surface to volume ratio[5], which enhances their targeting capabilities. Thus, NP based drug delivery systems have a great potential to achieve efficient targeting of cells and molecules in inflammation and cancer conditions [6]. In this section, challenges of drug delivery in microcirculation, influence of red blood cells, vessel geometry effect and target selection will be discussed respectively.

Current challenges in the study of drug delivery and distribution

Recent theoretical modelling works demonstrated decreased particle adhesion probability with increased flow rate [7-9]. Due to bioethical regulations and complex physiological conditions, it is challenging to quantify the particle delivery process *in vivo*. Most of the current studies are carried out in flow chambers or channels [10-11] and these results are applicable to large blood vessels but not to microvasculature. Microvasculature refers to part of the circulatory system consisting of capillaries, arterioles, and venules [12]. Microvasculature parameters such as vascular geometry, target-receptor expression levels and flow shear rate must be considered while performing *in vitro* tests. Study on specific receptor mediated binding of nano drug carriers under various physiologically relevant conditions help in understanding the methodologies to enhance targeted delivery efficacy and provides a tool to determine the actual drug bioavailability.

Distribution of drug carriers under the influence of RBC

Blood is a complex bio-fluid consisting of RBCs, monocytes, platelets, proteins etc. Blood flow in microvasculature is a two-phase flow as the vessel diameter becomes comparable to the size of RBCs. *In vitro* studies on RBC mediated particle delivery have to consider various *in vivo* microvasculature parameters, such as Fåhræus–Lindqvist effect [13], Segre–Silberberg effect [14-15], CFL formation [16-18], vessel geometry/bifurcations [19] and blunt velocity profile [20-23].

RBCs have a biconcave shape of ~8 μm diameter and ~2 μm thickness, and are highly deformable [18, 24]. The flexible RBCs migrate radially towards the centre region in microvessels based on various hemorheology factors such as shear rate, viscosity, hematocrit concentration, RBC aggregation and deformability. This results in a RBC concentrated core region and a cell-free plasma layer near the vascular wall called CFL [16, 24-25]. Particles flowing along with RBCs can diffuse towards these CFL and this will influence their distribution and binding dynamics across a channel [26-28].

The deformable RBCs aggregate to form a fast moving core at the centre of the channel while the stiffer cells and particles marginate to the near wall CFL region of the microvessel. This localization of particles closer to the vessel wall would increase the particle density in the CFL region. The targeted binding of drug carriers to diseased cells would be enhanced by this process. In this work we consider the influence of RBCs on 210 nm and 2 μm particle distribution.

Influence of vessel geometry in drug carrier distribution

Human circulatory system consists of large blood vessels such as arteries and veins (~15-0.5 mm), and smaller vessels such as arterioles, venules (100-500 μm) and capillaries (~10 μm). The distribution of drug particles in a real vascular network having hierarchical geometry will depend on local shear rate, flow velocity, pressure and volume [29]. Our study considers the distribution of nano and micron sized particles in a branching channel that mimics the geometry and flow conditions of a dividing vascular network. A comparison of particle binding density between the branching and the straight channel geometry is performed to examine non-uniform distribution of particles at vessel bifurcation with and without RBCs. In order to study the effect of a difference in flow velocity distribution between daughter channels on particle binding, we conducted flow tests on channel geometries that would produce asymmetric flow rate distribution in the two daughter channels.

Specificity in drug carrier targeting

Specificity in targeting is introduced by applying ligand-receptor chemistry in the microfluidic platform. The biomimetic chip is coated with intercellular adhesion molecule 1 (ICAM-1) protein, a cell-surface glycoprotein member of the Ig super-family. Under inflammatory conditions, interaction between endothelial cells and blood constituents occur by the up-regulation of intercellular adhesion molecules such as ICAM-1 on the surface of endothelial cells and leukocyte [30-31]. This mediates the targeted migration of leukocytes into specific areas of inflammation [32]. Various ICAM-1 based therapeutic agents for cancer immunotherapy and other modes of treatment are used nowadays [33-34]. Here anti-ICAM-1 coated 210 nm and 2 μm particles are used as a model system to study the influence of RBCs and vascular geometry on particle delivery.

This work studies binding distribution of anti-ICAM-1 coated particles on ICAM-1 protein coated microfluidic platform. Influence of particle size (210 nm and 2 μm), shear rates, vessel geometries (straight and branched channels) and RBCs are examined. Microfluidic device fabrication, protein coating (on channels and particles) and their characterization, and testing are described in methods section. Results and discussions under aforementioned conditions are given thereafter. Finally, the conclusion and future work are presented.

Materials and methods

Materials

Human ICAM-1/CD54 MAb (Clone BBIG-I1) Mouse IgG1, ICAM-1/human IgG1 Fc chimera, biotinylated anti-human ICAM-1 (clone BBIG, mouse IgG1 κ) and Normal Goat

IgG biotinylated control was purchased from R&D Systems, Minneapolis, MN). Protein G was bought from Biovision, Milpitas, CA. Horseradish peroxidase (HRP)-conjugated rat anti-mouse κ -light chain monoclonal antibody, neutrAvidin coated fluorescent yellow-green polystyrene 210 nm particles, Block-Aid, Amplex Ultra Red reagent and biotinylated-HRP was purchased from Invitrogen Carlsbad, CA. Mouse anti-human ICAM-1 monoclonal IgG1 antibody (clone 15.2) was got from Ancell, Bayport, MN and HRP-conjugated rat anti-mouse IgG1 monoclonal antibody from BD Biosciences San Jose, CA. Bovine serum albumin (BSA), 3-aminopropyltrimethoxysilane was bought from Sigma Aldrich, St Louis, MO. Streptavidin coated 2 μ m fluorescent green polystyrene particles was purchased from Bangs Laboratories Inc., IN and polydimethylsiloxane from Dow Corning, Midland MI. Single donor human whole blood and plasma was bought from Innovative Research Inc..

Fabrication of microfluidic device

The required microfluidic design is photo-lithographically patterned on a silicon wafer using SU-8 2050 photoresist. Microfluidic devices are fabricated using Sylgard 184 PDMS. PDMS base is mixed with its cure at 1:10 (v/v) ratio following the basic techniques in soft lithography [35]. The PDMS mixture is poured on the silicon wafer, which acts as the master template. The hard PDMS layer is peeled out after baking and the features are inspected. The microfluidic device is made by binding the PDMS pattern on a clean glass slide after exposing them to oxygen (O_2) plasma. The flow channels are 100 μ m wide and 100 μ m in height. Both straight and bifurcating features are included in the design. The bifurcating channels have a branching angle of 60°.

ICAM-1 functionalized PDMS substrate

PDMS devices were coated with ICAM-1 as previously reported[10]. After binding with glass the PDMS microfluidic devices were silanized with 3-aminopropyltrimethoxysilane to improve protein adsorption. After washing the device with an adsorption buffer (0.1M $NaHCO_3$, pH 9.2), the devices were incubated for 2 hrs at room temperature with saturating concentration of protein G in adsorption buffer (100 μ g/ml). ICAM-1 Fc chimera protein solution in PBS (100 nM) was introduced after washing the substrates three times with PBS to remove any excess protein G. The devices were incubated with ICAM-1 for 1 hr at room temperature. The microfluidic chips were purged with 1% BSA containing 0.05% Tween20 one hour prior to testing.

Substrate ICAM-1 density characterization

In order to quantify the ICAM-1 protein density on the PDMS surface, ELISA was performed using an HRP-conjugated anti mouse IgG1 antibody. ELISA reaction was carried out in a 12-well plate and PDMS coated 22 mm circular glasses were used. The technique for substrate ICAM-1 characterization was performed as reported in literature [10].

Silicone isolators (Grace Bio Labs) were used to assure that the same volume of reagents were applied on PDMS coated glass as in the microfluidic device, to maintain the same surface area to volume ratio. Once the PDMS coated cover slips were coated with ICAM-1 Fc protein, they were blocked before silicone isolators were removed. This was followed by incubation with mouse anti-ICAM-1 at 2 μ g/ml for 1 hr at 4 C, and incubation with HRP-

conjugated mouse antibody (1:1000 dilution). Each steps were followed by washing with ice cold PBS. After the final wash step, the cover slips were placed in the well plate. Amplex Ultra Red reagent was used to initiate the ELISA reaction and was allowed to incubate for 10 min at room temperature. Fluorescence was measured on a microplate reader at 544 nm excitation/590 nm emission. The readings were compared to a calibration curve and the ICAM-1 surface density was calculated.

Anti-ICAM-1 coated micro/nano particles

Neutravidin coated 210 nm and streptavidin coated 2 μ m fluorescent particles were diluted to 10^{10} and 10^8 particles/ml respectively using Block-Aid and sonicated for 5 minutes. Biotinylated antibody (anti-ICAM-1, control or both) was added next after diluting the particles in 1% BSA. The 210 nm particles were diluted to 10^9 particles/ml and the 2 μ m particles were brought down to 10^7 particles/ml and the antibody concentration was kept to a total of 10 μ g/ml. Particles were incubated for 3 hours while shaking at room temperature and the unbound antibody was removed by centrifugation. The particles were washed in 1% BSA solution to remove any leftover unbound antibody and then diluted to working concentration for the flow tests. Particle concentration was analyzed on a microplate reader at 485 nm excitation/530 nm emission and compared to a calibration curve constructed from stock particle solution.

Particle anti-ICAM-1 density characterization

ELISA was performed using HRP conjugated anti-mouse k-light chain specific monoclonal antibody to characterize the particle surface antibody density. The specificity of the reagent to mouse antibody light chain provides a direct measurement of the anti-ICAM-1 binding sites available on the particle. Particles were incubated with 5% HRP conjugated anti-mouse k-light chain specific monoclonal antibody for 30 minutes, followed by washing with 1% BSA solution and clearing out of unbound antibody through centrifugation. 50 μ l of the particle solution were loaded on a 96-well plate and the particle concentration was analyzed. Then 50 μ l of Amplex Ultra Red reagent was added to each well and the HRP-substrate reaction was allowed to proceed for 10 minutes at room temperature. The fluorescence intensity of the particle sample with Amplex Ultra Red reagent was observed on a microplate reader at 544 nm excitation and 590 nm emission. The fluorescence intensities were converted to the number of HRP molecule using the calibration curves prepared using biotinylated-HRP conjugation to the neutravidin/streptavidin coated particles. Assuming a 1:1 binding ratio between anti-ICAM-1 and secondary antibody, the anti-ICAM-1 density on the particles were determined. In order to make sure the reaction mechanism and kinetics involved for anti-ICAM-1 binding on particle and while performing ELISA are same in the nano and micron sized particles, we compared the fluorescence intensity for similar anti-ICAM-1 density case of both particle sizes. This helps to make sure that the different protein and antibody binding reactions involved while performing ELISA doesn't vary based on particle size and other possible steric hindrance factors.

Microfluidic flow test cases

The microfluidic device is designed to mimic the geometry of a typical microvasculature. The design contains both straight and branching sections. The bifurcating angle was decided

from measurements on arterial microcirculation system, theoretical values based on Murray's law and the bifurcation angle relationships of minimum work principle [36]. Particle binding density at straight and branching region are calculated separately. The area considered to be the bifurcation section starts from the point where straight channels begins to bifurcate and ends in the daughter channel at a length of 2.5 times the vessel diameter from the apex of bifurcation (Fig. 1). This was based on the principle that it takes about 2 times the distance of vessel diameter for the re establishment of parabolic flow after bifurcation [37].

Anti-ICAM-1 coated particles were flown through ICAM-1 modified microfluidic devices at different shear rates between 200 and 1600 s^{-1} . This corresponds to physiologically relevant values observed in the microvessels [38-39]. The binding session was followed by a PBS only flushing session to remove unbound particles and to study particle detachment. This is performed at the same shear rate used to study particle attachment. The shear rate of flow in daughter channels are half that of the parent channel after branching, as they have the same dimension as the parent channel and also the daughter channels are of the same length. The particle concentration is kept at $10^8/ml$ and $10^6/ml$ for 210 nm and 2 μm particles respectively. The duration of flow were fixed at 15 and 20 minutes for 210 nm and 2 μm particles respectively. These time periods and particle concentrations were decided to accommodate all particle binding studies to a window where the binding rate was steady and the binding density could be practically quantified. Since the particle concentration and flow time are kept constant for all shear rates, the numbers of total particles introduced into the channels increase with shear rate. This factor is considered while calculating the particle binding density. The results were normalized to a total particle count of $10^6/flow$ case for all studies performed. The normalization process is explained in the supplementary information (Table S7). To compare the effect of particle size on binding, few flow cases were performed at $10^6/ml$ concentration for 210 nm particles.

Particle binding density was computed from confocal scans of the bottom surface of the channel. Time lapse imaging was performed in order to determine the attachment and detachment profile of the particles under different flow conditions. Analysis of particle binding was performed on a high resolution laser confocal fluorescence microscope (FV1000-IX81, Olympus). The particle binding density is computed at the centre section of the bottom channel surface. Centre section of the channel is decided by excluding areas within 25% of the channel width from edges. Flow conditions are more stable at the centre compared to the edges of the channel and thus the variation in particle binding density is low here.

Flow tests were performed with particles diluted in pure buffer and whole blood with 25% RBC hematocrit, which represents the average hematocrit in microvessels [40]. Whole blood with 40% RBC concentration was brought down to 25% by diluting in human blood plasma. The RBC flow case studies the influence of RBCs on particle diffusion and binding in microvessels. Blood plasma can contain soluble factors like CAM molecules which vary from donor to donor and can possibly affect the binding of particles on ICAM-1 modified substrates [41-42]. Thus the same pool of plasma and whole blood was used for all RBC

flow test cases and the tests were performed the same day to normalize the effect of these soluble factors.

Fluid flow was generated using a programmable syringe pump (Harvard Apparatus), which controls the volumetric flow rate that is proportional to the wall shear rate. The wall shear rate was derived from the volumetric flow rate using the following relation:

$$\dot{\gamma} = \left(6Q/H^2W\right) (1+H/W) f * (H/W)$$

Where H is the height and W is the width of the microfluidic device. 'f' is a geometry factor derived from the ratio of width to height. In this study, a microfluidic channel with a height and width of 100 μm is used, thus $f=0.5928$ [43].

The effect of asymmetric flow between daughter branches on particle binding was also studied. For daughter channels with identical width and height, the relationship between flow rate and resistance is simplified to $L_a Q_a = L_b Q_b$ [44] (L_a, Q_a, L_b and Q_b are the length and flow rate of the daughter channels a and b respectively). Based on this, a change in length in one of the daughter channel would proportionally change the flow rate in that channel. A change in flow rate would translate to a direct proportional change in shear rate of flow (Table 1 on page 25). Channels were designed to generate different flow distribution in the two daughter channels as shown in Table 1. The shear rate in one of the daughter channel is half of the other. Only straight sections of both the parent and daughter channels (after branching) were scanned to quantify the particle binding density in this case. Particle binding was quantified at the same distance from branching apex for both the daughter channels.

Results and Discussion

Characterization of particle receptor and PDMS substrate ligand protein densities

ICAM-1 coating density of the microfluidic channels were kept the same for all flow cases. It was determined by applying ELISA on PDMS coated glass slides as described before [10]. ICAM-1 density on our microfluidic channels was measured to be 121 ± 12 sites/ μm^2 . NeutrAvidin coated 210 nm and Streptavidin coated 2 μm particles were functionalized with anti-ICAM-1 based on biotin-avidin chemistry. The anti-ICAM-1 coating density on the particle was determined using ELISA. Complete saturation of antibody coating on 210 nm particles produced 239.3 ± 25 anti-ICAM-1/particle. This was brought down to 157.9 ± 19 and 78.6 ± 9 anti-ICAM-1/particle. This corresponds to $1905.3 \pm 199/\mu\text{m}^2$ for the maximum antibody density case, followed by 1257.1 ± 151 and 625.8 ± 71 anti-ICAM-1/ μm^2 . The 2 μm particles were tuned to have a density of 12184.1 ± 264 and 2767.9 ± 103 anti-ICAM-1/particle which corresponds to 1199.2 ± 25 and 272.2 ± 10 anti-ICAM-1/ μm^2 respectively. Particle coating density was tuned using biotinylated goat IgG control antibody.

Specificity of anti-ICAM-1 coated particle binding to ICAM-1 coated surface

Specificity of particle binding to ICAM-1 coated surface was studied by comparing the binding of anti-ICAM-1 coated particles to negative control case (Fig 2). Particles coated

with biotinylated goat IgG control antibody was used as negative control. 210 nm and 2 μm sized particles were coated with 1905.3 and 1199.2 anti-ICAM-1/ μm^2 respectively. Both pure buffer and RBC 25% cases were performed at a shear rate of 200 s^{-1} . Particles specifically bound to ICAM-1 coated microfluidic channel with around ten times higher density when compared to the negative control case, for both pure buffer and with RBCs cases.

210 nm particle binding distribution

In order to study the binding and flow dynamics of particles in the nanometer scale, studies were performed on 210 nm particles suspended in both pure buffer and whole blood (25% RBC). Binding of particles on both straight and bifurcating regions of the channel was examined. Three different anti-ICAM-1 particle coating densities (1905.3, 1257.1 and 625.8 anti-ICAM-1/ μm^2) were studied and flow tests were conducted for a shear rate range of 200-1600 s^{-1} .

It is observed that the binding density of 210 nm particles decreases with shear rate in both straight and branching channels for pure buffer case (Fig 3 A and C). However, for the RBC 25% flow case (Fig 3 B and D) an increase in binding density is observed for the 1257.1 and 625.8 anti-ICAM-1/ μm^2 cases till 550 s^{-1} shear rate. However, for the 1905.3 anti-ICAM-1/ μm^2 particle case the highest particle binding density occurs at a shear rate of 200 s^{-1} . The particle binding density data before normalization (Fig S1) shows an increase in particle binding density till 550 s^{-1} for all the three particle anti-ICAM-1 coating densities. This anomaly before and after normalization for the 1905.3 anti-ICAM-1/ μm^2 particle case could be because of the particle binding density reaching a saturation, i.e. all the ICAM-1 receptor spots available for binding on the wall is occupied by anti-ICAM-1 coated particles and there are no more accessible ICAM-1 receptors on the channel. To verify this we extended the flow time (to 45 minutes) for the 200 s^{-1} case and observed the particle binding density reaching a saturation at around the same value seen for 550 s^{-1} case before normalization (Fig S1 C).

Fig 4 shows confocal images of particle binding in the branching section of the channel for different anti-ICAM-1 coating densities at 550 s^{-1} shear rate for 210 nm particles under RBC 25% flow case. The RBC 25% flow case show ~2-3 times enhanced binding density when compared to pure buffer flow case for 210 nm particles, with the difference decaying with increase in shear rate (Fig 3). This increase in particle binding density can be explained by the availability of more particles to the near wall region when flowing with RBCs. The presence of RBCs push out particles from the channel centre towards the near wall CFL region, thereby bringing more particles closer to the ICAM-1 coated surface. In order to confirm this phenomenon, the concentration of free suspending 210 nm particles in the CFL region was compared between the pure buffer and RBC 25% flow cases. Confocal images of particle flow at 200, 550 and 900 s^{-1} shear rates were collected. Images captured from 1 μm above the bottom surface of the channel to a height of 5 μm in the z direction were summed together. This compilation shows the fluorescence intensity emitted by the particle flow present in the CFL region. Analysis of the stacked confocal fluorescence images (Fig S3) showed an increase in fluorescence intensity for the RBC 25% flow case compared to the

pure buffer case for all three shear rates. This confirms higher particle concentration, thus the localization of free suspending 210 nm particles in the near wall CFL region when flowing with RBCs. As the shear rate increases from 550 s^{-1} to the higher shear regime, particle binding density drops for the RBC case like the pure buffer case. This is likely because the localization of particles to the CFL saturates or drag force produced by flow shear exceeds adhesion force between ICAM-1 and anti-ICAM-1 receptor ligands. The decrease in particle binding density with an increase in shear rate can be explained as the binding process being in a reaction limited regime as explained in *Namdee et al's* and *Charoenphol et al's* work [45-46]. A similar drop in particle binding density for 210 nm particles with increase in shear rate is also observed in Haun and Hammer's work [10].

The binding density also increases with particle anti-ICAM-1 density for all flow cases. Higher antibody coating density on the 210 nm particles provides a better possibility of enough ligand-receptor bond formation to assure firm attachment of the particles to the ICAM-1 coated surface [10, 47]. In terms of channel geometry, 10% higher NP binding density is observed at bifurcations compared to straight channels. Flow disturbances or alteration of flow at bifurcation regions lead to enhanced particle collision with the wall, which enhance binding [8, 48-50].

2 μm particle binding distribution

To study micron sized particle distribution, binding of 2 μm particles were studied in pure buffer and whole blood case at 25% RBC. Particle binding density was evaluated for both straight and branching channels. Flow tests were performed using particles of 1199.2 and 272.2 anti-ICAM-1/ μm^2 coating densities.

Like the 210 nm particles the binding density of 2 μm particles also decreases with shear rate in both straight and branching section of the channel for pure buffer case (Fig 5 A and C). They show around 6-10 times increase in binding density when suspended in 25% RBC depending on the shear rate (Fig 5 B and D) when compared to the pure buffer case. The shear rate range under study leads to formation of CFL during RBC flow. The accumulation of RBCs in the centre core region of the channel pushes the 2 μm particles toward the near wall CFL. This increases the concentration of 2 μm particles near the channel surface. Accumulation of particles in the CFL leads to overall increase in particle binding observed for the 2 μm particles. However, as the flow shear rate increases above 550 s^{-1} the particle binding density decreases for the 2 μm particles. At higher shear rates the larger drag force can easily wash away larger attached particles regardless of anti-ICAM-1 coating density. Work by *Patil et al.* found the shear rate required to set in motion a firmly adhered microsphere to decrease with increasing microsphere diameter [51]. This is a result of same shear producing higher drag force on larger particles. Thus shear rate based detachment effects are more dominant in the larger 2 μm particles compared to the 210 nm ones. This is consistent with existing literature [51-53]. Detachment profile of 210 nm and 2 μm particles in Fig S4 and S5 gives a better understanding of this phenomenon.

Similar to the 210 nm particles the binding density of 2 μm particles also increase with particle anti-ICAM-1 coating density. At 200 s^{-1} shear rate there is about five time increase in particle binding density for the 1199.2/ μm^2 case over the 272.2/ μm^2 anti-ICAM-1 density

case (Fig. 5 B and D). However such antibody coating density induced increase in binding density decays at higher shear rates for the 2 μm particles. It is observed that at 1600 s^{-1} shear rate both particle anti-ICAM-1 coating densities show similar binding density. At lower shear rates the particle binding is influenced more by the receptor-ligand interaction. However at higher shear rates the 2 μm particle binding process is influenced more by the availability of particles near the wall region and the detachment of particles by the high flow shear rate. Like the 210 nm particles ~10% increase in binding density is also observed for the 2 μm particles at the branching region. Fig. 6 shows confocal images of particle binding in the branching section of the channel for different anti-ICAM-1 coating densities at 200 s^{-1} shear rate for RBC 25% flow case.

The binding profiles of 210 nm and 2 μm particles at different shear rates demonstrate that there are two mechanisms involved in particle attachment. Generally, the particle attachment process consists of particle diffusion/margination toward the wall and ligand-receptor bond formation upon contact. The increase in shear rate decreases the time available for particle to diffuse/marginate toward the wall, thus decreasing the binding density. The time available for ligand-receptor reaction also play a role in particle attachment [54-55]. When the anti-ICAM-1 coated particles come in contact with the ICAM-1 functionalized substrate, binding reaction between the receptor and ligand protein occurs. At lower shear rates particles have longer time period for multivalent bond formation, while it decreases when the flow happens at high shear rates. This explains the decreased particle binding density observed with an increase in shear rate. Higher antibody coating density helps faster formation of enough ligand-receptor bonds to assure firm attachment, thus increase binding density.

On the other hand, the particle detachment process is the competition between drag force and bonding force from ligand-receptor pairs. At low to medium shear rates, higher ligand coating density helps particle from being detached. However, very large drag force dominates at high shear rate, especially for 2 μm particle. A very rough estimate of the drag

force on a sphere is: $F_D = \frac{\pi}{8} \rho C_D d^2$, where C_D is the drag coefficient and d is the particle diameter. The drag force acting on a sphere increases linearly with the area of the sphere. Meanwhile, the ligand-receptor bonding force does not increase linearly with area of the sphere due to the point contact nature of the sphere-surface interaction. Thus 2 μm particles can be easily washed away at high shear rates, as explained by the low binding density as well as higher detachment rate. In comparison, the 210 nm particles experience much smaller drag force even at high shear rate.

Comparison between binding of 210 nm particle and 2 μm particles

A comparison is performed on the binding density characteristics of 210 nm and 2 μm particles with similar anti-ICAM-1 densities (1257.1 and 1199.2 anti-ICAM-1/ μm^2 for 210 nm particles and 2 μm particles respectively) in this section.

Fig 7 A and B compares the particle binding density for 210 nm and 2 μm particles for pure buffer and RBC 25% flow case respectively. For the RBC flow case 2 μm particles show higher binding for shear rates up to 550 s^{-1} . This is constant with work by *Namdee et al* [46] who also observes increased binding for 2 μm particles compared to 200 nm when flowing

in a 30% RBC solution. For higher shear rates the larger drag force acting on bigger 2 μm particles leads to detachment and thus produce less particle binding compared to 210 nm particles.

For the pure buffer case the binding density of 210 nm particles is 2-3 times higher than 2 μm particles. However, it should be noted that this study was conducted at a particle concentration of $10^8/\text{ml}$ for the 210 nm particles and $10^6/\text{ml}$ for the 2 μm particles. In order to understand the effect of this 100 times increase in particle concentration on binding density, we also did flow tests at $10^6/\text{ml}$ particle concentration for 210 nm particles. It was observed that both the pure buffer and RBC 25% flow cases produced particle binding that didn't vary significantly with changes in factors such as shear rate, particle antibody density or flow with RBCs (data not shown). To understand this we measured the localization of 210 nm particles at this concentration near the wall region for the pure buffer and RBC 25% case using confocal microscope scanning. No significant fluorescence signal was observed near the wall region when compared to the $10^8/\text{ml}$ case (Fig S3), which indicates the lack of particle localization to near wall CFL region. Our study was conducted at a particle concentration of $10^8/\text{ml}$ for the 210 nm particles and $10^6/\text{ml}$ for the 2 μm particles and the results were normalized to 10^6 particles/flow case for both particle sizes. Thus this 100 times higher 210 nm particle concentration should have translated to the higher particle binding density observed in the pure buffer case. The work by *Namdee et al* [46] also observes an increase in particle binding density with increased particle concentration for the pure buffer case.

Fig. 7C compares the magnitude of increase in particle binding density for RBC 25% whole blood case compared to the pure buffer case for the 2 μm and 210 nm particles with similar anti-ICAM-1 density. This is done by calculating the ratio of increase in particle binding density for the RBC 25% case over the pure buffer case under the same shear rates for both 2 μm and 210 nm particles. 2 μm particles show almost three times increase in binding ratio when flowing with RBCs compared to similar 210 nm particle case for shear rate up to 550 s^{-1} . Even at high shear rates above 550 s^{-1} 2 μm particles show almost twice the binding ratio compared to 210 nm particles, although detachment becomes dominant as shear rate increases.

Prominent binding is observed for the 2 μm particle for RBC 25% flow case when compared to 210 nm particles due to size based enhanced particle margination to the CFL. Particles or cells marginate toward the near wall cell free region when flowing along with RBCs [45, 56-58]. This occurs because of their interaction with RBCs and the deformation of the RBCs in flow. The collision between the deforming RBCs during flow easily pushes out particles or cells of size comparable to RBCs to the cell free plasma region. In *Eckstein et al's* work, a size selective enhanced exclusion of beads of diameter greater than 2.2 μm was observed [59]. In this confined region the interaction between the RBCs and particles increases the collision between the anti-ICAM-1 coated particles and the ICAM-1 coated PDMS surface and this leads to increased particle binding. Similar phenomenon was observed in other works [45-46, 60]. Comparatively only a smaller percentage of 210 nm particles marginate toward the near wall region and most of them tend to flow along with RBCs in the core region because of their smaller size [59]. This along with their smaller size compared to the

CFL (2-10 μm) [17, 61] produces less increase in particle binding density compared to the 2 μm particle case.

Daughter channels with asymmetric flow velocity

In micro circulation, daughter channels can have difference in flow velocities between them after branching [19]. In order to study the effect of this asymmetric flow distribution between daughter branches on particle binding, we conducted tests in channels of geometries that produce this effect. The parent and daughter channels were of the same cross sectional area, but of different lengths. This would produce a variation in flow rate between the daughter channels such that the shear rate of one daughter channel would be half of the other. Daughter channel 'b' had half the length of channel 'a' (Figure along with Table 1) for this purpose. Table 1 lists the shear rates of flow in parent and the two daughter channels for the three flow cases performed. Flow tests were conducted for 210 nm and 2 μm particles having an anti-ICAM-1 coating density of $1905.3/\mu\text{m}^2$ and $1199.2/\mu\text{m}^2$, suspended in 25% hematocrit whole blood.

The binding density for 210 nm particles at a concentration of $10^8/\text{ml}$ is given in Fig 8 A. For the three flow cases at a shear rate of 200, 900 and 1600 s^{-1} in the parent channel, higher particle binding density is observed in the daughter channel when compared to the parent channel. Daughter channel 'a' have $1/3^{\text{rd}}$ and 'b' have $2/3^{\text{rd}}$ the shear rate of the parent channel and between them channel 'b' has twice the shear rate of channel 'a'. The daughter channel 'a' shows almost 2 times higher binding density than channel 'b'. This can be explained by channel 'a' having half the flow shear rate of channel 'b'. 210 nm particles show similar increased binding density with decreased shear rate pattern as discussed earlier (Fig. 3).

For the 2 μm particles almost similar particle binding density was observed in parent and daughter channels for all shear rates other than for 1600, 1066.6 and 900 s^{-1} (Fig 8 B) after normalization. These results match well with what we saw for RBC 25% case of 2 μm particles at different shear rates for a particle anti-ICAM-1 density of $1199.2/\mu\text{m}^2$ (Fig 5). It is observed that the particle binding density begins to decrease dramatically for shear rate above 600 s^{-1} . This is because of large drag force from these higher shear rates acting on the particle, which leads to decreased receptor ligand reaction and also increased particle detachment.

In flow channels where the daughter branches have different flow velocities, there might be a preferential, non-linear distribution of RBCs/particles to the daughter branch with the faster flow [62-64]. Thus the daughter channel with higher flow velocity/shear rate ends up receiving more RBCs/particles. We didn't observe such a preferential flow of particles to the daughter channel having the higher shear rate. This could be because our particle size is much smaller when compared to the flow channel cross section. Our 2 μm particle is only 0.02 times the size of the channel with a length and height of 100 μm each (210 nm particle becomes more insignificant). The above mentioned non-linear distribution are prominent only when the diameter of RBC/particle is of the same range as the channel diameter [63].

Conclusion

The binding density of anti-ICAM-1 coated 210 nm and 2 μm particles on ICAM-1 modified PDMS microfluidic devices is characterized in this work. The study employs various factors that influence particle distribution and binding such as flow shear rate, particle size, flow along with RBCs, vessel geometry, antibody coating density on the particle, particle concentration and effect of asymmetric flow distribution between daughter channels.

The particle binding densities for both 210 nm and 2 μm particles decrease with increased shear rate for pure buffer case. This can be explained by the decreased available time for particle to diffuse/marginate toward the wall under increased flow rate. RBCs play an important role in particle binding and distribution pattern. Both 210 nm and 2 μm particles show enhanced binding density at 25% hematocrit RBC flow. 210 nm particles showed 2-3 fold increase in binding under blood flow till a shear rate of 550 s^{-1} and 2 times increase in binding for much higher shear rates when compared to the pure buffer case. Similarly, 2 μm particles show around 6-10 fold increase in binding for shear rates up to 550 s^{-1} and around 4 times increase in binding for much higher shear rates when compared to the pure buffer case. The steep drop in binding density observed for the RBC 25% flow case of 2 μm particles beyond a shear rate of 550 s^{-1} is a result of high shear flow induced large drag force acting on the bigger 2 μm particles leading to their detachment. The smaller 210 nm particles have much lower drag force acting on them compared to the 2 μm particles.

In terms of vessel geometry, both particles show slight increase in binding density at the bifurcation region compared to the straight channels. This is observed for both pure buffer and RBC 25% flow case. Disturbance of flow at bifurcation region leads to enhanced particle collision with the wall and results in higher particle binding density. This contributes to the enhanced binding observed at branching section. Higher antibody coating density helps faster formation of enough ligand-receptor bonds to assure firm attachment of particles. Higher particle anti-ICAM-1 coating density thus increases binding density, except for high shear rate cases for 2 μm particles where shear based detachment drag force nullifies the enhancement brought by increased antibody density.

The results produced in our study can be related to clinically relevant drug delivery systems like liposomes[65], trimethyl chitosan (TMC)[66] and Poly(lactic-co-glycolic acid) (PLGA) based particles [67]. Our model system is spherical in shape and made of polymerized polystyrene, similar to structures generated through conventional techniques of particle fabrication like emulsion, precipitation and polymerization of formulations. The application of ligand based targeting is currently largely employed in such platforms to attain specific attachment and receptor mediated endocytosis to diseased cells. The ligand functionalization provides better therapeutic performance especially for macromolecules that are hard to enter cells on their own [66-68]. Such targeted platforms also expresses better uptake by cells based on vascular permeability [69], tumor penetrability [69] and ligand-receptor density and affinity [70-71]. The particle sizes in our study roughly cover the size range of established delivery platforms [66-67, 72].

Our work helps to determine the transport properties of drug carriers in the microvasculature. From this work we conclude that 2 μm particles have better binding efficiency based on number count and particle volume, for low to medium shear rate flow regions. For disease conditions where a higher particle concentration or dosage is acceptable (drug toxicity not an issue) and higher shear flows are involved, the smaller particles in the 200 nm scale would be more suitable. Properties like the enhanced particle margination and binding to the wall at high particle flow concentration observed in this work favours the use of NPs. Other advantages like the ability to be better retained in tissues via the enhanced permeability and retention effect, longer circulation period and better targeting ability are also in favour of NPs.

When designing targeted vascular drug carriers, various parameters have to be considered like the disease condition, permissible drug toxicity based particle concentration, reticuloendothelial system evading properties etc. This work is part of a project to develop customized biomimetic microfluidic experimental platform that mimics specific microvasculature conditions based on disease state and physiological conditions. These goals are to be achieved by coating the microfluidic channels with endothelial cells to mimic vascular morphology and to mimic disease condition by introducing specific cytokines. Thus a more physiologically relevant test condition can be set up for studying nano/micro drug carrier distribution and binding.

Supplementary Material

Refer to Web version on PubMed Central for supplementary material.

Acknowledgments

The authors acknowledge the supports of this work from National Science Foundation (NSF) CAREER grant CBET-1113040, NSF CBET-1067502, and National Institute of Health (NIH) grant EB015105.

References

1. Langer R. Drug Delivery and Targeting. *Nature*. 1998; 392:9–10.
2. Packhaeuser CB, et al. In situ forming parenteral drug delivery systems: an overview. *European Journal of Pharmaceutics and Biopharmaceutics*. 2004; 58(2):445–455. [PubMed: 15296966]
3. Singh R, Lillard JW Jr. Nanoparticle-based targeted drug delivery. *Experimental and Molecular Pathology*. 2009; 86(3):215–223. [PubMed: 19186176]
4. Cho K, et al. Therapeutic Nanoparticles for Drug Delivery in Cancer. *Clinical Cancer Research*. 2008; 14(5):1310–1316. [PubMed: 18316549]
5. Greg Light, SS.; Park, Eun-Jung; Drane, Denise. Student understanding of “surface-area- to-volume ratio” and its relationship to property change in the nano-science engineering context. 2010.
6. Suri S, Fenniri H, Singh B. Nanotechnology-based drug delivery systems. *Journal of Occupational Medicine and Toxicology*. 2007; 2(1):16. [PubMed: 18053152]
7. Shah S, et al. Modeling Particle Shape-Dependent Dynamics in Nanomedicine. *Journal of Nanoscience and Nanotechnology*. 2011; 11(2):919–928. [PubMed: 21399713]
8. Tan J, et al. The influence of size, shape and vessel geometry on nanoparticle distribution. *Microfluidics and Nanofluidics*. 2013; 14(1-2):77–87. [PubMed: 23554583]
9. Liu Y, Shah S, Tan J. Computational Modeling of Nanoparticle Targeted Drug Delivery. *Reviews in Nanoscience and Nanotechnology*. 2012; 1(1):66–83.

10. Haun JB, Hammer DA. Quantifying Nanoparticle Adhesion Mediated by Specific Molecular Interactions. *Langmuir*. 2008; 24(16):8821–8832. [PubMed: 18630976]
11. Kona S, et al. Biodegradable nanoparticles mimicking platelet binding as a targeted and controlled drug delivery system. *International Journal of Pharmaceutics*. (0).
12. <http://www.thefreedictionary.com/microvasculature>
13. Fåhræus R, Lindqvist T. The Viscosity of the blood in narrow capillary tubes. *American Journal of Physiology -- Legacy Content*. 1931; 96(3):562–568.
14. YANG BH, et al. Migration of a sphere in tube flow. *Journal of Fluid Mechanics*. 2005; 540:109–131.
15. Segré G, Silberberg A. Behaviour of macroscopic rigid spheres in Poiseuille flow Part 2. Experimental results and interpretation. *Journal of Fluid Mechanics*. 1962; 14(01):136–157.
16. Harry L G. The microcirculatory society Eugene M. Landis award lecture: The microrheology of human blood. *Microvascular Research*. 1986; 31(2):121–142. [PubMed: 3517596]
17. Kim S, et al. The cell-free layer in microvascular blood flow. *Biorheology*. 2009; 46(3):181–189. [PubMed: 19581726]
18. McHedlishvili G, Maeda N. Blood Flow Structure Related to Red Cell Flow: Determinant of Blood Fluidity in Narrow Microvessels. *The Japanese Journal of Physiology*. 2001; 51(1):19–30. [PubMed: 11281993]
19. Pries AR, Secomb TW, Gaehtgens P. Biophysical aspects of blood flow in the microvasculature. *Cardiovascular Research*. 1996; 32(4):654–667. [PubMed: 8915184]
20. William I R. Ratio of red cell velocities near the vessel wall to velocities at the vessel center in cerebral microcirculation, and an apparent effect of blood viscosity on this ratio. *Microvascular Research*. 1972; 4(1):98–101. [PubMed: 5036683]
21. Reinke W, Johnson P, Gaehtgens P. Effect of shear rate variation on apparent viscosity of human blood in tubes of 29 to 94 microns diameter. *Circulation Research*. 1986; 59(2):124–132. [PubMed: 3742742]
22. Gaehtgens P, Meiselman HJ, Wayland H. Velocity profiles of human blood at normal and reduced hematocrit in glass tubes up to 130 μ diameter. *Microvascular Research*. 1970; 2(1):13–23. [PubMed: 5523911]
23. Yasuhiko Sugii SN, Okamoto Koji. In vivo PIV measurement of red blood cell velocity field in microvessels considering mesentery motion. *Physiological Measurement*. 2002; 23(2)
24. Popel AS JP. Microcirculation and hemorheology. *Annual Review of Fluid Mechanics*. 2005; 37:43–69.
25. Ho Seong Ji, J.Y.L.a.S.J.L. In-vitro study on the hemorheological characteristics of chicken blood in microcirculation. *Rheology Journal*. 2007; 19:89–95.
26. Nanne EE, Aucoin CP, Leonard EF. Shear Rate and Hematocrit Effects on the Apparent Diffusivity of Urea in Suspensions of Bovine Erythrocytes. *ASAIO Journal*. 2010; 56(3):151–156. 10.1097/MAT.0b013e3181d4ed0f. [PubMed: 20335796]
27. Aarts P, Heethaar R, Sixma J. Red blood cell deformability influences platelets-- vessel wall interaction in flowing blood. *Blood*. 1984; 64(6):1228–1233. [PubMed: 6498337]
28. Goldsmith HL, G S. Mason, Particle motions in sheared suspensions XIII. The spin and rotation of disks. *Journal of Fluid Mechanics*. 1962; 12(01):88–96.
29. Mayrovitz HN, Tuma RF, Wiedeman MP. Relationship between microvascular blood velocity and pressure distribution. *American Journal of Physiology - Heart and Circulatory Physiology*. 1977; 232(4):H400–H405.
30. Gimbrone MA, Nagel T, Topper JN. Biomechanical activation: an emerging paradigm in endothelial adhesion biology. *The Journal of Clinical Investigation*. 1997; 99(8):1809–1813. [PubMed: 9109423]
31. Zhai Y, et al. LIGHT, a novel ligand for lymphotoxin beta receptor and TR2/HVEM induces apoptosis and suppresses in vivo tumor formation via gene transfer. *The Journal of Clinical Investigation*. 1998; 102(6):1142–1151. [PubMed: 9739048]
32. Min J-K, et al. TNF-Related Activation-Induced Cytokine Enhances Leukocyte Adhesiveness: Induction of ICAM-1 and VCAM-1 via TNF Receptor-Associated Factor and Protein Kinase C-

- Dependent NF- κ B Activation in Endothelial Cells. *The Journal of Immunology*. 2005; 175(1): 531–540. [PubMed: 15972689]
33. Kanwar JR, et al. Requirements for ICAM-1 immunogene therapy of lymphoma. *Cancer Gene Ther*. 2003; 10(6):468–476. [PubMed: 12768192]
 34. Hiroaki Tanaka MY, Sunami Takeshi, Masaichi Ohira, K. Hirakawa-Y.S. Chung, Lipid-mediated gene transfection of intercellular adhesion molecule-1 suppresses the peritoneal metastasis of gastric carcinoma. *International Jjournal of Molecular Medicine*. 2002; 10(5)
 35. McDonald JC, Whitesides GM. Poly(dimethylsiloxane) as a Material for Fabricating Microfluidic Devices. *Accounts of Chemical Research*. 2002; 35(7):491–499. [PubMed: 12118988]
 36. Lee J, Lee S. Murray's law and the bifurcation angle in the arterial micro- circulation system and their application to the design of microfluidics. *Microfluidics and Nanofluidics*. 2010; 8(1):85–95.
 37. Lew HS, Fung YC. Entry flow into blood vessels at arbitrary Reynolds number. *Journal of Biomechanics*. 1970; 3(1):23–38. [PubMed: 5521528]
 38. Nagaoka T, Yoshida A. Noninvasive Evaluation of Wall Shear Stress on Retinal Microcirculation in Humans. *Investigative Ophthalmology & Visual Science*. 2006; 47(3):1113–1119. [PubMed: 16505049]
 39. Patrizia Nigro, J.-i.A.; Berk, Bradford C. Flow Shear Stress and Atherosclerosis: A Matter of Site Specificity. *Antioxidants & Redox Signaling*. 2011; 15(5):1405–1414. [PubMed: 21050140]
 40. Pries AR, Secomb TW, Gaehtgens P. Structure and hemodynamics of microvascular networks: heterogeneity and correlations. *American Journal of Physiology - Heart and Circulatory Physiology*. 1995; 269(5):H1713–H1722.
 41. Gearing AJH, Newman W. Circulating adhesion molecules in disease. *Immunology Today*. 1993; 14(10):506–512. [PubMed: 7506035]
 42. Blankenberg S, et al. Circulating Cell Adhesion Molecules and Death in Patients With Coronary Artery Disease. *Circulation*. 2001; 104(12):1336–1342. [PubMed: 11560847]
 43. Son Y. Determination of shear viscosity and shear rate from pressure drop and flow rate relationship in a rectangular channel. *Polymer*. 2007; 48(2):632–637.
 44. Chau L, Doran M, Cooper-White J. A novel multishear microdevice for studying cell mechanics. *Lab on a Chip*. 2009; 9(13):1897–1902. [PubMed: 19532965]
 45. Charoenphol P, Huang RB, Eniola-Adefeso O. Potential role of size and hemodynamics in the efficacy of vascular-targeted spherical drug carriers. *Biomaterials*. 2010; 31(6):1392–1402. [PubMed: 19954839]
 46. Namdee K, et al. Margination Propensity of Vascular-Targeted Spheres from Blood Flow in a Microfluidic Model of Human Microvessels. *Langmuir*. 2013; 29(8):2530–2535. [PubMed: 23363293]
 47. Tan J, et al. Coupled particulate and continuum model for nanoparticle targeted delivery. *Computers & Structures*. 2013; 122(0):128–134. [PubMed: 23729869]
 48. Zhang Z KC, Donohue JF, Kim CS. Comparison of micro- and nano-size particle depositions in a human upper airway model. *J Aerosol Sci*. 2005; 36:211–233.
 49. Prabhakarparandian B, et al. Bifurcations: Focal Points of Particle Adhesion in Microvascular Networks. *Microcirculation*. 2011; 18(5):380–389. [PubMed: 21418388]
 50. Lamberti G, et al. Adhesive interaction of functionalized particles and endothelium in idealized microvascular networks. *Microvascular Research*. 2013; 89:107–114. (0). [PubMed: 23557880]
 51. Shinde Patil VR, C.J.C. Yun YH, Slack SM, Goetz DJ. Particle diameter influences adhesion under flow. *Biophys Journal*. 2001; 80(4):1733–1743.
 52. P Decuzzi FG, Granaldi A, Curcio A, Causa F. Flow chamber analysis of size effects in the adhesion of spherical particles. *International Journal of Nanomedicine*. 2007; 2(4):689–696. [PubMed: 18203435]
 53. Goldman AJ, Cox RG, Brenner H. Slow viscous motion of a sphere parallel to a plane wall—II Couette flow. *Chemical Engineering Science*. 1967; 22(4):653–660.
 54. Goldsmith, HL.; M, S. The microrheology of dispersions. In: Eirich, FR., editor. *Rheology, Theory, and Applications*. Vol. 4. Academic Press; New York: 1967. p. 85-250.

55. Calderon, Andres J.; Silvia Muro, VM.; Eckmann, David M. Flow dynamics, binding and detachment of spherical carriers targeted to ICAM-1 on endothelial cells. *Biorheology*. 2009; 46:323–341. [PubMed: 19721193]
56. Abbitt KB, Nash GB. Rheological properties of the blood influencing selectin- mediated adhesion of flowing leukocytes. *American Journal of Physiology - Heart and Circulatory Physiology*. 2003; 285(1):H229–H240. [PubMed: 12623791]
57. Gentile F, et al. The margination propensity of spherical particles for vascular targeting in the microcirculation. *Journal of Nanobiotechnology*. 2008; 6(1):9. [PubMed: 18702833]
58. Tan J, Thomas A, Liu Y. Influence of red blood cells on nanoparticle targeted delivery in microcirculation. *Soft Matter*. 2012; 8(6):1934–1946. [PubMed: 22375153]
59. Eckstein EC, Tilles AW, Millero FJ Iii. Conditions for the occurrence of large near-wall excesses of small particles during blood flow. *Microvascular Research*. 1988; 36(1):31–39. [PubMed: 3185301]
60. Melder RJ, et al. Selectin- and integrin-mediated T-lymphocyte rolling and arrest on TNF-alpha-activated endothelium: augmentation by erythrocytes. *Biophysical Journal*. 1995; 69(5):2131–2138. [PubMed: 8580357]
61. Maeda N, et al. Erythrocyte flow and elasticity of microvessels evaluated by marginal cell-free layer and flow resistance. *American Journal of Physiology - Heart and Circulatory Physiology*. 1996; 271(6):H2454–H2461.
62. Fenton B, Wilson D, Cokelet G. Analysis of the effects of measured white blood cell entrance times on hemodynamics in a computer model of a microvascular bed. *Pflügers Archiv*. 1985; 403(4):396–401. [PubMed: 4011392]
63. Yen RT, Y.C.F. Effect of velocity of distribution on red cell distribution in capillary blood vessels. *The American journal of physiology*. 1978; 09:H251–7. [PubMed: 686194]
64. Fung Y-C. Stochastic flow in capillary blood vessels. *Microvascular Research*. 1973; 5(1):34–48. [PubMed: 4684755]
65. Allen TM, Cullis PR. Liposomal drug delivery systems: From concept to clinical applications. *Advanced Drug Delivery Reviews*. 2013; 65(1):36–48. [PubMed: 23036225]
66. Mourya VK, Inamdar N. Trimethyl chitosan and its applications in drug delivery. *Journal of Materials Science: Materials in Medicine*. 2009; 20(5):1057–1079. [PubMed: 19112609]
67. Danhier F, et al. PLGA-based nanoparticles: An overview of biomedical applications. *Journal of Controlled Release*. 2012; 161(2):505–522. [PubMed: 22353619]
68. Lammers T, et al. Drug targeting to tumors: Principles, pitfalls and (pre-) clinical progress. *Journal of Controlled Release*. 2012; 161(2):175–187. [PubMed: 21945285]
69. Rakesh KJ, Triantafyllos S. Delivering nanomedicine to solid tumors. *Nature Reviews Clinical Oncology*. 2010; 7(11):653–664.
70. Park JW, et al. Anti-HER2 Immunoliposomes: Enhanced Efficacy Attributable to Targeted Delivery. *Clinical Cancer Research*. 2002; 8(4):1172–1181. [PubMed: 11948130]
71. Orcutt KD, et al. Effect of Small-Molecule–Binding Affinity on Tumor Uptake In Vivo: A Systematic Study Using a Pretargeted Bispecific Antibody. *Molecular Cancer Therapeutics*. 2012; 11(6):1365–1372. [PubMed: 22491799]
72. Torchilin VP. Multifunctional nanocarriers. *Advanced Drug Delivery Reviews*. 2006; 58(14):1532–1555. [PubMed: 17092599]

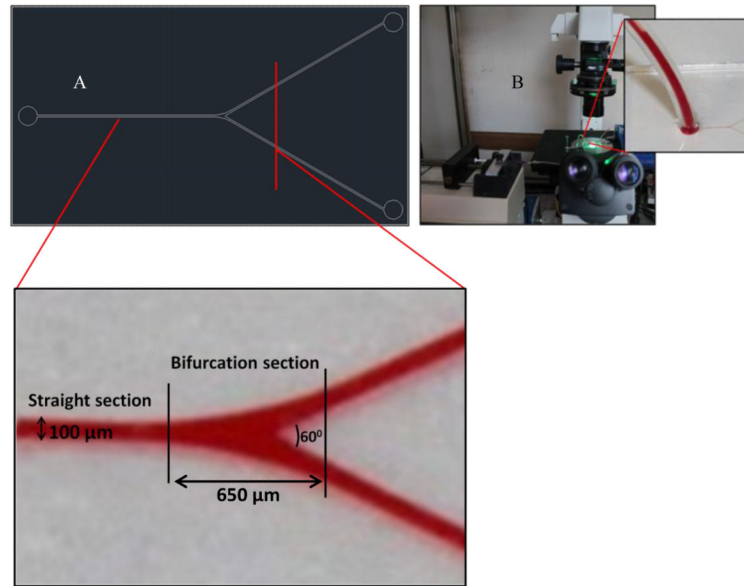


Figure 1.

(A) CAD design of microchannel geometry, enlarged part illustrates the straight and bifurcation section of the channel; (B) The flow test set-up.

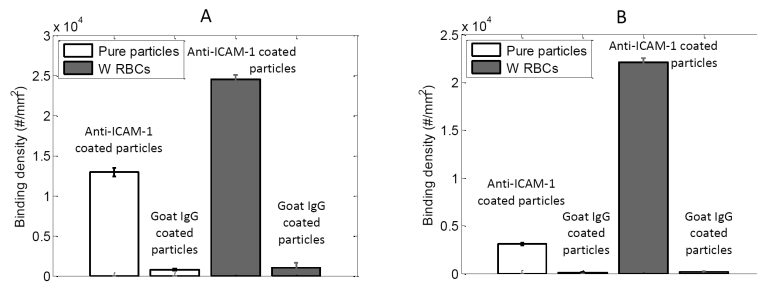


Figure 2. Binding density of anti-ICAM-1 and negative control (Goat IgG control) antibody coated (A) 210 nm particles and (B) 2 μm particles under 200 s⁻¹ shear rate for both pure buffer and RBC 25% flow cases.

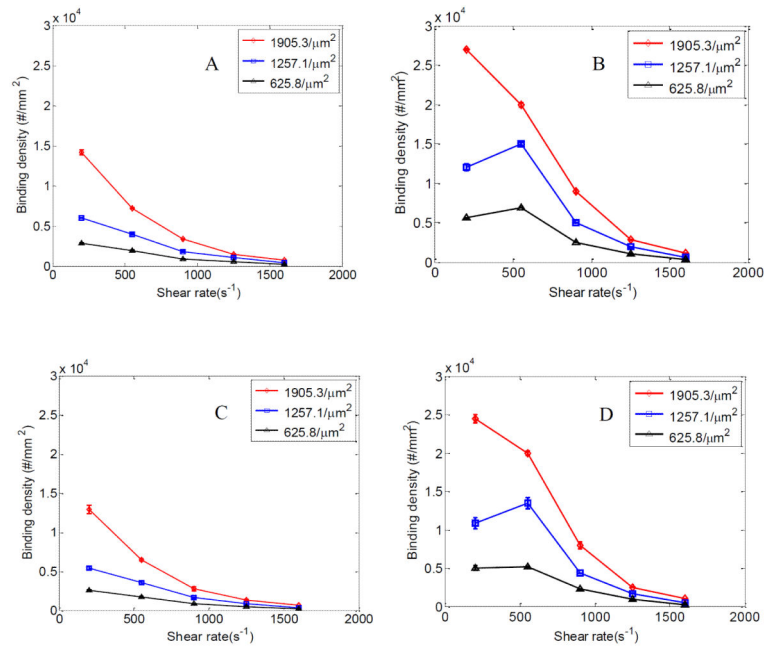


Figure 3. Normalized particle binding density ($\#/mm^2$) at shear rates between 200-1600 s^{-1} ; at branching section of channels under (A) pure buffer flow and (B) RBC flow for 210 nm particles; at straight section of channels under (C) pure buffer flow and (D) RBC flow for 210 nm particles. Binding densities are plotted for 1905.3, 1257.1 and 625.8 anti-ICAM-1/ μm^2 particle antibody densities. Error bars represent standard deviation for three independent flow cases each.

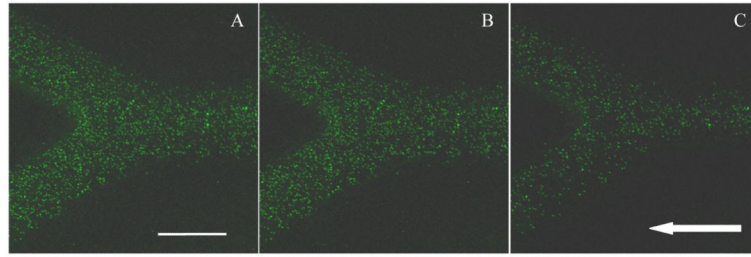


Figure 4. Confocal fluorescence images showing adhered 210 nm particles in ICAM-1 coated branched channel for RBC 25% case under 550 s^{-1} shear rate and three anti-ICAM-1 particle coating densities: (A) $1905.3/\mu\text{m}^2$; (B) $1257.1/\mu\text{m}^2$ and (C) $625.8/\mu\text{m}^2$ case. Arrow represents the flow direction (Scale bar: $100 \mu\text{m}$)

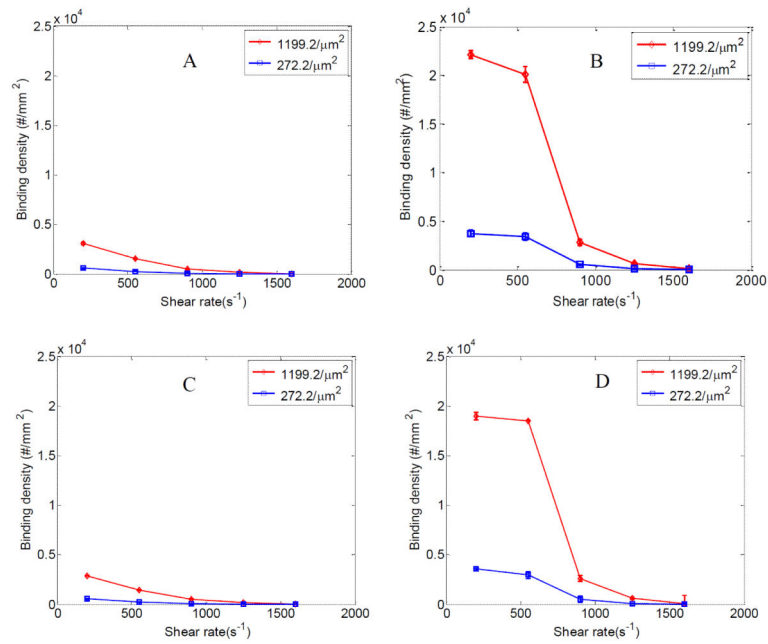


Figure 5. Normalized particle binding density ($\#/mm^2$) at shear rates between 200-1600 s^{-1} ; at branching section of channels under (A) pure buffer flow and (B) RBC 25% flow for 2 μm particles; at straight section of channels under (C) pure buffer flow and (D) RBC 25% flow for 2 μm particles. Binding densities are plotted for two different anti-ICAM-1 particle coating densities; 1199.2 and 272.2 anti-ICAM-1/ μm^2 . Error bars represent standard deviation for three independent flow cases each.

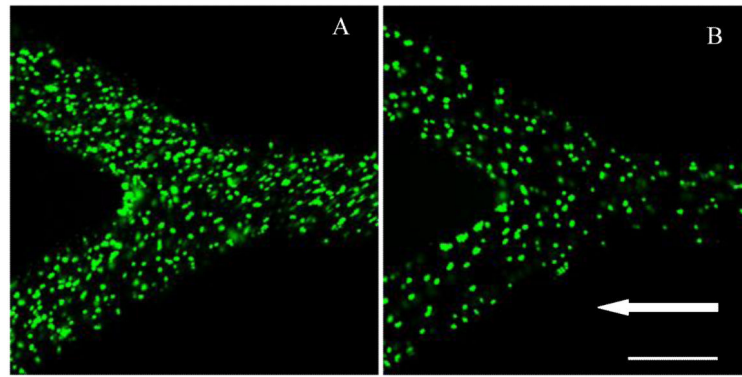


Figure 6. Confocal fluorescence image showing distribution of anti-ICAM-1 coated 2 μm particles in a branched channel for RBC 25% case under different shear rates and anti-ICAM-1 particle density respectively; (A) 200 s^{-1} , $1199.2/\mu\text{m}^2$; (B) 200 s^{-1} , $272.2/\mu\text{m}^2$. Arrow represents the flow direction (Scale bar: $100 \mu\text{m}$)

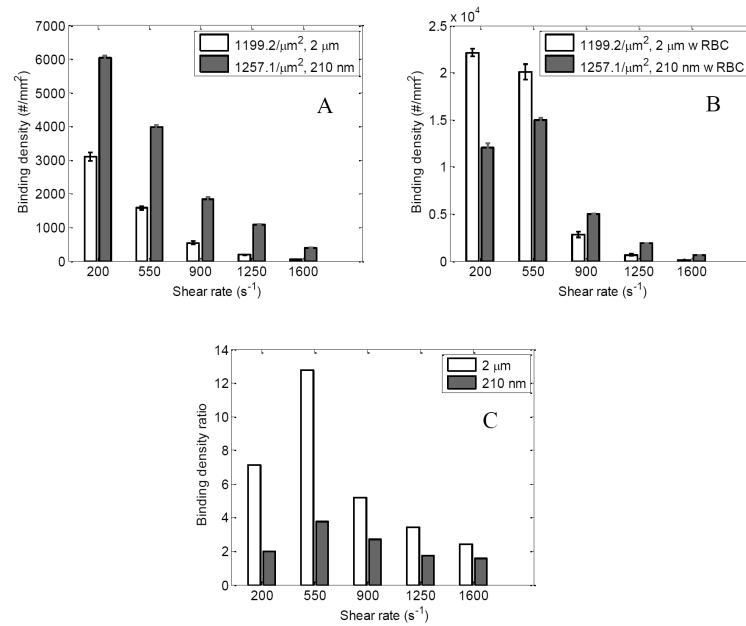


Figure 7. Normalized particle binding density ($\#/mm^2$) for 210 nm ($1257.1 \text{ anti-ICAM-1}/\mu m^2$) and 2 μm ($1199.2 \text{ anti-ICAM-1}/\mu m^2$) particles are compared for (A) pure buffer flow case and (B) RBC 25% flow case at different shear rates; (C) Comparing ratio of particle binding density of RBC flow case to pure buffer flow case for 210 nm ($1257.1 \text{ anti-ICAM-1}/\mu m^2$) and 2 μm ($1199.2 \text{ anti-ICAM-1}/\mu m^2$) particles at different shear rates;

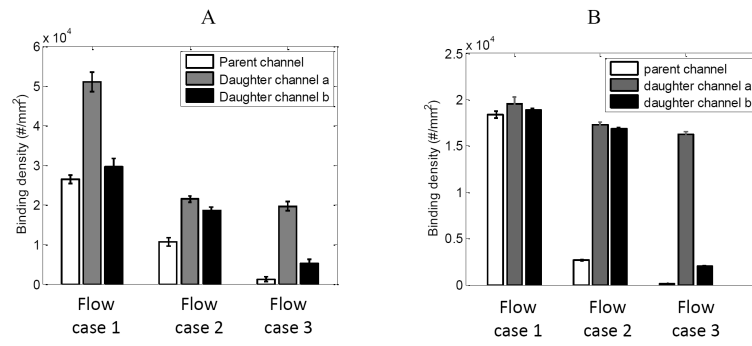



Figure 8. Normalized particle binding density in parent channel and daughter channels a and b for the asymmetric flow case under RBC flow for (A) 210 nm particles at 1905.3 anti-ICAM-1/ μm^2 and (B) 2 μm particles at 1199.2 anti-ICAM-1/ μm^2 .

Table 1

Shear rates in the parent channel and in daughter channels a and b for the different flow cases studied. Image shows the top view of the flow channel design that produces asymmetric flow in daughter channels



Flow case	Shear rate in parent channel	Shear rate in daughter channel a	Shear rate in daughter channel b
1	200	66.6	133.3
2	900	300	600
3	1600	533.3	1066.6